Computers and Mathematics with Applications 69 (2015) 518–529

Contents lists available at ScienceDirect

Computers and Mathematics with Applications

journal homepage: www.elsevier.com/locate/camwa

A D3Q27 multiple-relaxation-time lattice Boltzmann method for turbulent flows

K. Suga *, Y. Kuwata, K. Takashima, R. Chikasue

Department of Mechanical Engineering, Osaka Prefecture University, Sakai, Osaka 599–8531, Japan

ARTICLE INFO

Article history:
Received 5 July 2014
Received in revised form 17 November 2014
Accepted 25 January 2015
Available online 16 February 2015

Keywords:
D3Q27
Lattice Boltzmann equation
Multiple-relaxation-time
Turbulent flow

ABSTRACT

A three-dimensional twenty-seven (D3Q27) discrete velocity multiple-relaxation-time lattice Boltzmann method is developed. The proposed scheme is validated in fully developed turbulent channel, pipe and porous medium flows through direct and large eddy simulations. The direct numerical simulation of the turbulent channel flow confirms that the present scheme is as reliable as the spectrum method for simulating turbulence. Through the large eddy simulations of the pipe and porous medium flows, the present scheme shows its satisfactory accuracy for simulating turbulent flows bounded by circular walls that is failed by the three-dimensional nineteen (D3Q19) model.

1. Introduction

The lattice Boltzmann method (LBM) is now recognized as a powerful method for a Navier–Stokes solver due to its distinctive computational features. Indeed, the LBM is easy for coding, intrinsically parallelizable, and applicable to complex geometries straightforwardly. The most common LBM is the single-relaxation-time approximation based model that is written in the BGK form [1] and called lattice BGK (LBGK) model. This model is simple enough and has been widely applied in many flow cases from micro (see [2,3] for reviews) to turbulent flows (e.g. [4–10]). However, the solutions by the LBGK model often become unstable in complex flows at finite Knudsen or high Reynolds numbers. To overcome these difficulties, the multiple-relaxation-time (MRT) scheme proposed by d'Humiéres et al. [11,12] is useful to stabilize the solution and to obtain satisfactory results (e.g. [3,13,9,14]) because the MRT model allows the usage of an independently optimized relaxation-time for each physical process as Lallemand and Luo [15] discussed.

Another well known issue is that the LBM cannot be completely rotation and frame invariant. Dubois and Lallemand [16] and Augier et al. [17] discussed the method that improved the rotation invariance of the MRT LBM up to fourth order accuracy for acoustic waves. Dellar [18] showed that LBM produced non-Galilean invariant viscous stress arising from the absence of a moment tensor proportional to the cube of the fluid velocity and proposed to correct the defect. There have been many other discussions on those topics (e.g., [19–22]). Although such defects in invariance does not always visibly devastate flow simulations, some obvious difficulties in simulating turbulent flows can be found in the literature. It has been reported that insufficient isotropy is sometimes visible in simulating turbulent axisymmetric flows [23–25] by the square grid LBM. (Note that the present study only focuses on the square grid LBM.) Indeed, Kang and Hassan [24] reported that the three-dimensional nineteen (D3Q19) discrete velocity model produced unphysical secondary currents in turbulent pipe flows and violated Galilean invariance in square duct turbulence while the three-dimensional twenty-seven (D3Q27) model did

* Corresponding author.
E-mail address: suga@me.osakafu-u.ac.jp (K. Suga).

http://dx.doi.org/10.1016/j.camwa.2015.01.010
0898-1221/

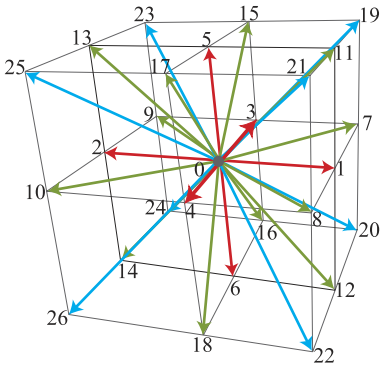

Fig. 1. D3Q27 discrete velocity model of the square grid lattice Boltzmann method.

not. By performing the error term analysis proposed by Holdych et al. [26], the present authors [27] proved that this was because the error terms, which include Reynolds stresses, distribute cyclically in the circumferential direction and produce false forces in particular directions in the D3Q19 model. The same effect can be observed in the three-dimensional fifteen discrete velocity (D3Q15) model but the error magnitudes in the D3Q27 model are substantially small.

After all, what we need for simulating complex turbulent flows is a D3Q27 MRT LBM. However, to the best of the authors' knowledge, such a model has not been reported in the literature. (Note that Premnath and Banerjee [28] studied a central moment LBM that looks similar to an MRT LBM.) Therefore, the present study tries to develop an MRT lattice Boltzmann equation (LBE) for the D3Q27 discrete velocity model and to optimize the collision tensor for stably simulating turbulent flows. Then, validation of the proposed scheme is performed in the fully developed turbulent channel, pipe and porous medium flows within the framework of direct and large eddy simulations.

2. D3Q27 MRT lattice Boltzmann equation

The LBE is obtained by discretizing the velocity space of the Boltzmann equation into a finite number of discrete velocities $\boldsymbol{e}_\alpha\{\alpha = 0, 1, \ldots, Q-1\}$. With a proper set of discrete velocities, the LBE recovers the continuum Navier–Stokes equations by the Chapman–Enskog expansion (see [29]). (It is also true for the MRT schemes [15].) Although many schemes to discretize the velocity space have been proposed, for three-dimensional (3-D) flows, the present study focuses on so called the three-dimensional twenty-seven (D3Q27) discrete velocity model which is illustrated in Fig. 1. Table 1 lists the sound speed c_S, the discrete velocity $\boldsymbol{e}_\alpha$ and the weight parameter w_α in the model with $c = \delta x/\delta t$ where δx and δt are the lattice spacing and the time step, respectively. The MRT LBM [12] transforms the distribution function in the velocity space to the moment space by the transformation matrix $\boldsymbol{M}$. Since the moments of the distribution function correspond directly to flow quantities, the moment representation allows us to perform the relaxation processes with different relaxation-times according to different time-scales of various physical processes. The evolution equation for the particle distribution function $\boldsymbol{f}$ is thus written as

$$|\boldsymbol{f}\ (\boldsymbol{r}_i + \boldsymbol{e}_\alpha \delta t, t + \delta t)\rangle - |\boldsymbol{f}\ (\boldsymbol{r}_i, t)\rangle = -\boldsymbol{M}^{-1}\widehat{\boldsymbol{S}}\left[|\boldsymbol{m}(\boldsymbol{r}_i, t)\rangle - |\boldsymbol{m}^{(eq)}(\boldsymbol{r}_i, t)\rangle\right] + |\boldsymbol{F}(\boldsymbol{r}_i, t)\rangle. \tag{1}$$

where $\boldsymbol{r}_i$ is the position vector of node i, $\widehat{\boldsymbol{S}}$ is the collision matrix, $\boldsymbol{m}$ is the moment, $\boldsymbol{F}$ represents an external body force and the notation for the column vector (known as the ket vector) such as $|\boldsymbol{f}\rangle$ represents

$$|\boldsymbol{f}\ (\boldsymbol{r}_i, t)\rangle = (f_0(\boldsymbol{r}_i, t), f_1(\boldsymbol{r}_i, t), \ldots, f_{Q-1}(\boldsymbol{r}_i, t))^T. \tag{2}$$

The components of $\boldsymbol{F}$ are given as

$$F_\alpha = w_\alpha \rho \frac{\boldsymbol{e}_\alpha \cdot \boldsymbol{a}}{c_S^2}\delta t, \tag{3}$$

where ρ is the fluid density and $\boldsymbol{a}$ is the acceleration. Note that there is a more accurate expression for the force term discussed in [30]. The collision matrix $\widehat{\boldsymbol{S}}$ is diagonal: $\widehat{\boldsymbol{S}} = \mathrm{diag}(s_0, s_1, \ldots, s_{Q-1})$ and when $\boldsymbol{S} = \omega\boldsymbol{I}$ ($\boldsymbol{I}$: identity matrix, $\omega = 1/\tau$, $\tau(> 1/2)$, τ: relaxation time), Eq. (1) reduces to the lattice BGK equation.

The matrix $\boldsymbol{M}$ is a $Q \times Q$ matrix which linearly transforms the distribution function to the moment: $|\boldsymbol{m}\rangle = \boldsymbol{M} \cdot |\boldsymbol{f}\rangle$. The moments are the fluid density ρ, the momentum $\boldsymbol{j}$, the kinetic energy $\boldsymbol{e}$, etc. For the D3Q27 model, following Dubois and Lallemand [16], flow quantities are defined using the distribution function:
for the fluid density,

$$\tilde{m}_0 = \rho \equiv \sum_{\alpha=0}^{26} f_\alpha, \tag{4}$$

for the momentum,

$$\begin{cases} \tilde{m}_1 = j_x \equiv \sum_{\alpha=0}^{26} f_\alpha e_{\alpha x}, \\ \tilde{m}_2 = j_y \equiv \sum_{\alpha=0}^{26} f_\alpha e_{\alpha y}, \\ \tilde{m}_3 = j_z \equiv \sum_{\alpha=0}^{26} f_\alpha e_{\alpha z}, \end{cases} \tag{5}$$

for the kinetic energy,

$$\tilde{m}_4 = e \equiv \sum_{\alpha=0}^{26} \left(e_{\alpha x}^2 + e_{\alpha y}^2 + e_{\alpha z}^2\right) f_\alpha \tag{6}$$

for the second order tensor,

$$\begin{cases} \tilde{m}_5 = XX \equiv \sum_{\alpha=0}^{26} \left(2e_{\alpha x}^2 - e_{\alpha y}^2 - e_{\alpha z}^2\right) f_\alpha, \\ \tilde{m}_6 = WW \equiv \sum_{\alpha=0}^{26} \left(e_{\alpha y}^2 - e_{\alpha z}^2\right) f_\alpha, \end{cases} \tag{7}$$

$$\begin{cases} \tilde{m}_7 = XY \equiv \sum_{\alpha=0}^{26} \left(e_{\alpha x} e_{\alpha y}\right) f_\alpha, \\ \tilde{m}_8 = YZ \equiv \sum_{\alpha=0}^{26} \left(e_{\alpha y} e_{\alpha z}\right) f_\alpha, \\ \tilde{m}_9 = ZX \equiv \sum_{\alpha=0}^{26} \left(e_{\alpha z} e_{\alpha x}\right) f_\alpha, \end{cases} \tag{8}$$

for the fluxes of the energy and square of energy,

$$\begin{cases} \tilde{m}_{10} = \varphi_x \equiv 3 \sum_{\alpha=0}^{26} \left(e_{\alpha x}^2 + e_{\alpha y}^2 + e_{\alpha z}^2\right) e_{\alpha x} f_\alpha, \\ \tilde{m}_{11} = \varphi_y \equiv 3 \sum_{\alpha=0}^{26} \left(e_{\alpha x}^2 + e_{\alpha y}^2 + e_{\alpha z}^2\right) e_{\alpha y} f_\alpha, \\ \tilde{m}_{12} = \varphi_z \equiv 3 \sum_{\alpha=0}^{26} \left(e_{\alpha x}^2 + e_{\alpha y}^2 + e_{\alpha z}^2\right) e_{\alpha z} f_\alpha, \end{cases} \tag{9}$$

$$\begin{cases} \tilde{m}_{13} = \psi_x \equiv \frac{9}{2} \sum_{\alpha=0}^{26} \left(e_{\alpha x}^2 + e_{\alpha y}^2 + e_{\alpha z}^2\right)^2 e_{\alpha x} f_\alpha, \\ \tilde{m}_{14} = \psi_y \equiv \frac{9}{2} \sum_{\alpha=0}^{26} \left(e_{\alpha x}^2 + e_{\alpha y}^2 + e_{\alpha z}^2\right)^2 e_{\alpha y} f_\alpha, \\ \tilde{m}_{15} = \psi_z \equiv \frac{9}{2} \sum_{\alpha=0}^{26} \left(e_{\alpha x}^2 + e_{\alpha y}^2 + e_{\alpha z}^2\right)^2 e_{\alpha z} f_\alpha, \end{cases} \tag{10}$$

for the square and cube of the energy,

$$\tilde{m}_{16} = \varepsilon \equiv \frac{3}{2} \sum_{\alpha=0}^{26} \left(e_{\alpha x}^2 + e_{\alpha y}^2 + e_{\alpha z}^2\right)^2 f_\alpha, \tag{11}$$

$$\tilde{m}_{17} = e_3 \equiv \frac{9}{2} \sum_{\alpha=0}^{26} \left(e_{\alpha x}^2 + e_{\alpha y}^2 + e_{\alpha z}^2\right)^3 f_\alpha, \tag{12}$$

for the product of the second order tensor and the energy,

$$\begin{cases} \tilde{m}_{18} = XX_e \equiv \sum_{\alpha=0}^{26} \left(2e_{\alpha x}^2 - e_{\alpha y}^2 - e_{\alpha z}^2\right)\left(e_{\alpha x}^2 + e_{\alpha y}^2 + e_{\alpha z}^2\right) f_\alpha, \\ \tilde{m}_{19} = WW_e \equiv \sum_{\alpha=0}^{26} \left(e_{\alpha y}^2 - e_{\alpha z}^2\right)\left(e_{\alpha x}^2 + e_{\alpha y}^2 + e_{\alpha z}^2\right) f_\alpha, \end{cases} \tag{13}$$

$$\begin{cases} \tilde{m}_{20} = XY_e \equiv \sum_{\alpha=0}^{26} \left(e_{\alpha x} e_{\alpha y}\right)\left(e_{\alpha x}^2 + e_{\alpha y}^2 + e_{\alpha z}^2\right) f_\alpha, \\ \tilde{m}_{21} = YZ_e \equiv \sum_{\alpha=0}^{26} \left(e_{\alpha y} e_{\alpha z}\right)\left(e_{\alpha x}^2 + e_{\alpha y}^2 + e_{\alpha z}^2\right) f_\alpha, \\ \tilde{m}_{22} = ZX_e \equiv \sum_{\alpha=0}^{26} \left(e_{\alpha z} e_{\alpha x}\right)\left(e_{\alpha x}^2 + e_{\alpha y}^2 + e_{\alpha z}^2\right) f_\alpha \end{cases} \tag{14}$$

for the third order pseudo-vector and the totally antisymmetric tensor XYZ,

$$\begin{cases} \tilde{m}_{23} = \tau_x \equiv \sum_{\alpha=0}^{26} e_{\alpha x}\left(e_{\alpha y}^2 - e_{\alpha z}^2\right) f_\alpha, \\ \tilde{m}_{24} = \tau_y \equiv \sum_{\alpha=0}^{26} e_{\alpha y}\left(e_{\alpha z}^2 - e_{\alpha x}^2\right) f_\alpha, \\ \tilde{m}_{25} = \tau_z \equiv \sum_{\alpha=0}^{26} e_{\alpha z}\left(e_{\alpha x}^2 - e_{\alpha y}^2\right) f_\alpha, \end{cases} \tag{15}$$

$$\tilde{m}_{26} = XYZ \equiv \sum_{\alpha=0}^{26} \left(e_{\alpha x} e_{\alpha y} e_{\alpha z}\right) f_\alpha, \tag{16}$$

where $e_{\alpha x}$, $e_{\alpha y}$, $e_{\alpha z}$ are the components of $\boldsymbol{e}_\alpha$ in the $x-$, $y-$, z-directions, respectively. When the moments are written as $|\tilde{\boldsymbol{m}}\rangle = \tilde{\boldsymbol{M}} \cdot |\boldsymbol{f}\rangle$, the matrix $\tilde{\boldsymbol{M}}$ becomes

$$\tilde{\boldsymbol{M}} = \begin{pmatrix}
1 & 1 & 1 & 1 & 1 & 1 & 1 & 1 & 1 & 1 & 1 & 1 & 1 & 1 & 1 & 1 & 1 & 1 & 1 & 1 & 1 & 1 & 1 & 1 & 1 & 1 & 1 \\
1 & 0 & -1 & 0 & 0 & 0 & 1 & -1 & -1 & 1 & 1 & 0 & -1 & 0 & 1 & 0 & -1 & 0 & 1 & -1 & -1 & 1 & 1 & -1 & -1 & 1 & 0 \\
0 & 1 & 0 & -1 & 0 & 0 & 1 & 1 & -1 & -1 & 0 & 1 & 0 & -1 & 0 & 1 & 0 & -1 & 1 & 1 & -1 & -1 & 1 & 1 & -1 & -1 & 0 \\
0 & 0 & 0 & 0 & 1 & -1 & 0 & 0 & 0 & 0 & 1 & 1 & 1 & 1 & -1 & -1 & -1 & -1 & 1 & 1 & 1 & 1 & -1 & -1 & -1 & -1 & 0 \\
1 & 1 & 1 & 1 & 1 & 1 & 2 & 2 & 2 & 2 & 2 & 2 & 2 & 2 & 2 & 2 & 2 & 2 & 3 & 3 & 3 & 3 & 3 & 3 & 3 & 3 & 0 \\
2 & -1 & 2 & -1 & -1 & -1 & 1 & 1 & 1 & 1 & 1 & -2 & 1 & -2 & 1 & -2 & 1 & -2 & 0 & 0 & 0 & 0 & 0 & 0 & 0 & 0 & 0 \\
0 & 1 & 0 & 1 & -1 & -1 & 1 & 1 & 1 & 1 & -1 & 0 & -1 & 0 & -1 & 0 & -1 & 0 & 0 & 0 & 0 & 0 & 0 & 0 & 0 & 0 & 0 \\
0 & 0 & 0 & 0 & 0 & 0 & 1 & -1 & 1 & -1 & 0 & 0 & 0 & 0 & 0 & 0 & 0 & 0 & 1 & -1 & 1 & -1 & 1 & -1 & 1 & -1 & 0 \\
0 & 0 & 0 & 0 & 0 & 0 & 0 & 0 & 0 & 0 & 0 & 1 & 0 & -1 & 0 & -1 & 0 & 1 & 1 & 1 & -1 & -1 & -1 & -1 & 1 & 1 & 0 \\
0 & 0 & 0 & 0 & 0 & 0 & 0 & 0 & 0 & 0 & 1 & 0 & -1 & 0 & -1 & 0 & 1 & 0 & 1 & -1 & -1 & 1 & -1 & 1 & 1 & -1 & 0 \\
3 & 0 & -3 & 0 & 0 & 0 & 6 & -6 & -6 & 6 & 6 & 0 & -6 & 0 & 6 & 0 & -6 & 0 & 9 & -9 & -9 & 9 & 9 & -9 & -9 & 9 & 0 \\
0 & 3 & 0 & -3 & 0 & 0 & 6 & 6 & -6 & -6 & 0 & 6 & 0 & -6 & 0 & 6 & 0 & -6 & 9 & 9 & -9 & -9 & 9 & 9 & -9 & -9 & 0 \\
0 & 0 & 0 & 0 & 3 & -3 & 0 & 0 & 0 & 0 & 6 & 6 & 6 & 6 & -6 & -6 & -6 & -6 & 9 & 9 & 9 & 9 & -9 & -9 & -9 & -9 & 0 \\
b & 0 & -b & 0 & 0 & 0 & e & -e & -e & e & e & 0 & -e & 0 & e & 0 & -e & 0 & g & -g & -g & g & g & -g & -g & g & 0 \\
0 & b & 0 & -b & 0 & 0 & e & e & -e & -e & 0 & e & 0 & -e & 0 & e & 0 & -e & g & g & -g & -g & g & g & -g & -g & 0 \\
0 & 0 & 0 & 0 & b & -b & 0 & 0 & 0 & 0 & e & e & e & e & -e & -e & -e & -e & g & g & g & g & -g & -g & -g & -g & 0 \\
a & a & a & a & a & a & 6 & 6 & 6 & 6 & 6 & 6 & 6 & 6 & 6 & 6 & 6 & 6 & d & d & d & d & d & d & d & d & 0 \\
b & b & b & b & b & b & f & f & f & f & f & f & f & f & f & f & f & f & h & h & h & h & h & h & h & h & 0 \\
6 & -3 & 6 & -3 & -3 & -3 & 6 & 6 & 6 & 6 & 6 & -c & 6 & -c & 6 & -c & 6 & -c & 0 & 0 & 0 & 0 & 0 & 0 & 0 & 0 & 0 \\
0 & 3 & 0 & 3 & -3 & -3 & 6 & 6 & 6 & 6 & -6 & 0 & -6 & 0 & -6 & 0 & -6 & 0 & 0 & 0 & 0 & 0 & 0 & 0 & 0 & 0 & 0 \\
0 & 0 & 0 & 0 & 0 & 0 & 6 & -6 & 6 & -6 & 0 & 0 & 0 & 0 & 0 & 0 & 0 & 0 & 9 & -9 & 9 & -9 & 9 & -9 & 9 & -9 & 0 \\
0 & 0 & 0 & 0 & 0 & 0 & 0 & 0 & 0 & 0 & 0 & 6 & 0 & -6 & 0 & -6 & 0 & 6 & 9 & 9 & -9 & -9 & -9 & -9 & 9 & 9 & 0 \\
0 & 0 & 0 & 0 & 0 & 0 & 0 & 0 & 0 & 0 & 6 & 0 & -6 & 0 & -6 & 0 & 6 & 0 & 9 & -9 & -9 & 9 & -9 & 9 & 9 & -9 & 0 \\
0 & 0 & 0 & 0 & 0 & 0 & 1 & -1 & -1 & 1 & -1 & 0 & 1 & 0 & -1 & 0 & 1 & 0 & 0 & 0 & 0 & 0 & 0 & 0 & 0 & 0 & 0 \\
0 & 0 & 0 & 0 & 0 & 0 & -1 & -1 & 1 & 1 & 0 & 1 & 0 & -1 & 0 & 1 & 0 & -1 & 0 & 0 & 0 & 0 & 0 & 0 & 0 & 0 & 0 \\
0 & 0 & 0 & 0 & 0 & 0 & 0 & 0 & 0 & 0 & 1 & -1 & 1 & -1 & -1 & 1 & -1 & 1 & 0 & 0 & 0 & 0 & 0 & 0 & 0 & 0 & 0 \\
0 & 0 & 0 & 0 & 0 & 0 & 0 & 0 & 0 & 0 & 0 & 0 & 0 & 0 & 0 & 0 & 0 & 0 & 1 & -1 & 1 & -1 & -1 & 1 & -1 & 1 & 0
\end{pmatrix}, \tag{17}$$

Table 1
Parameters of the D3Q27 discrete velocity model.

Model	c_S/c	$\boldsymbol{e}_\alpha/c$	w_α
D3Q27	$1/\sqrt{3}$	(0, 0, 0)	$8/27(\alpha = 0)$
		$(\pm1, 0, 0)$, $(0, \pm1, 0)$, $(0, 0, \pm1)$	$2/27(\alpha = 1, \ldots, 6)$
		$(\pm1, \pm1, 0)$, $(\pm1, 0, \pm1)$, $(0, \pm1, \pm1)$	$1/54(\alpha = 7, \ldots, 18)$
		$(\pm1, \pm1, \pm1)$	$1/216(\alpha = 19, \ldots, 26)$

where $a = 1.5,\ b = 4.5,\ c = 12,\ d = 13.5,\ e = 18,\ f = 36,\ g = 40.5$ and $h = 121.5$. By the standard Gram–Schmidt procedure, $\widetilde{\boldsymbol{M}}$ can be orthogonalized and one can derive the transformation matrix $\boldsymbol{M}$. When $\widetilde{\boldsymbol{M}}_i$ and $\boldsymbol{M}_i$ denote the ith rows of $\widetilde{\boldsymbol{M}}$ and $\boldsymbol{M}$, respectively, $\boldsymbol{M}_k$ can be written as

$$\boldsymbol{M}_k = \widetilde{\boldsymbol{M}}_k - \sum_{i=0}^{k-1} \frac{\widetilde{\boldsymbol{M}}_k \cdot \boldsymbol{M}_i}{|\boldsymbol{M}_i|^2} \boldsymbol{M}_i \ (k \geq 4)\,. \tag{18}$$

Since the corresponding moments to $\widetilde{\boldsymbol{M}}_0, \ldots, \widetilde{\boldsymbol{M}}_3$ are ρ, j_x, j_y and j_z, respectively, and they are mutually independent, the orthogonalization procedure is enforced from the fourth row. Then, by applying Eq. (18), the transformation matrix $\boldsymbol{M}$ is derived as

$$\boldsymbol{M} = \begin{pmatrix}
1 & 1 & 1 & 1 & 1 & 1 & 1 & 1 & 1 & 1 & 1 & 1 & 1 & 1 & 1 & 1 & 1 & 1 & 1 & 1 & 1 & 1 & 1 & 1 & 1 & 1 & 1 \\
1 & 0 & -1 & 0 & 0 & 0 & 1 & -1 & -1 & 1 & 1 & 0 & -1 & 0 & 1 & 0 & -1 & 0 & 1 & -1 & -1 & 1 & 1 & -1 & -1 & 1 & 0 \\
0 & 1 & 0 & -1 & 0 & 0 & 1 & 1 & -1 & -1 & 0 & 1 & 0 & -1 & 0 & 1 & 0 & -1 & 1 & 1 & -1 & -1 & 1 & 1 & -1 & -1 & 0 \\
0 & 0 & 0 & 0 & 1 & -1 & 0 & 0 & 0 & 0 & 1 & 1 & 1 & 1 & -1 & -1 & -1 & -1 & 1 & 1 & 1 & 1 & -1 & -1 & -1 & -1 & 0 \\
-1 & -1 & -1 & -1 & -1 & -1 & 0 & 0 & 0 & 0 & 0 & 0 & 0 & 0 & 0 & 0 & 0 & 0 & 1 & 1 & 1 & 1 & 1 & 1 & 1 & 1 & -2 \\
2 & -1 & 2 & -1 & -1 & -1 & 1 & 1 & 1 & 1 & 1 & -2 & 1 & -2 & 1 & -2 & 1 & -2 & 0 & 0 & 0 & 0 & 0 & 0 & 0 & 0 & 0 \\
0 & 1 & 0 & 1 & -1 & -1 & 1 & 1 & 1 & 1 & -1 & 0 & -1 & 0 & -1 & 0 & -1 & 0 & 0 & 0 & 0 & 0 & 0 & 0 & 0 & 0 & 0 \\
0 & 0 & 0 & 0 & 0 & 0 & 1 & -1 & 1 & -1 & 0 & 0 & 0 & 0 & 0 & 0 & 0 & 0 & 1 & -1 & 1 & -1 & 1 & -1 & 1 & -1 & 0 \\
0 & 0 & 0 & 0 & 0 & 0 & 0 & 0 & 0 & 0 & 0 & 1 & 0 & -1 & 0 & -1 & 0 & 1 & 1 & 1 & -1 & -1 & -1 & -1 & 1 & 1 & 0 \\
0 & 0 & 0 & 0 & 0 & 0 & 0 & 0 & 0 & 0 & 1 & 0 & -1 & 0 & -1 & 0 & 1 & 0 & 1 & -1 & -1 & 1 & -1 & 1 & 1 & -1 & 0 \\
-4 & 0 & 4 & 0 & 0 & 0 & -1 & 1 & 1 & -1 & -1 & 0 & 1 & 0 & -1 & 0 & 1 & 0 & 2 & -2 & -2 & 2 & 2 & -2 & -2 & 2 & 0 \\
0 & -4 & 0 & 4 & 0 & 0 & -1 & -1 & 1 & 1 & 0 & -1 & 0 & 1 & 0 & -1 & 0 & 1 & 2 & 2 & -2 & -2 & 2 & 2 & -2 & -2 & 0 \\
0 & 0 & 0 & 0 & -4 & 4 & 0 & 0 & 0 & 0 & -1 & -1 & -1 & -1 & 1 & 1 & 1 & 1 & 2 & 2 & 2 & 2 & -2 & -2 & -2 & -2 & 0 \\
4 & 0 & -4 & 0 & 0 & 0 & -2 & 2 & 2 & -2 & -2 & 0 & 2 & 0 & -2 & 0 & 2 & 0 & 1 & -1 & -1 & 1 & 1 & -1 & -1 & 1 & 0 \\
0 & 4 & 0 & -4 & 0 & 0 & -2 & -2 & 2 & 2 & 0 & -2 & 0 & 2 & 0 & -2 & 0 & 2 & 1 & 1 & -1 & -1 & 1 & 1 & -1 & -1 & 0 \\
0 & 0 & 0 & 0 & 4 & -4 & 0 & 0 & 0 & 0 & -2 & -2 & -2 & -2 & 2 & 2 & 2 & 2 & 1 & 1 & 1 & 1 & -1 & -1 & -1 & -1 & 0 \\
0 & 0 & 0 & 0 & 0 & 0 & -1 & -1 & -1 & -1 & -1 & -1 & -1 & -1 & -1 & -1 & -1 & -1 & 1 & 1 & 1 & 1 & 1 & 1 & 1 & 1 & 4 \\
4 & 4 & 4 & 4 & 4 & 4 & -2 & -2 & -2 & -2 & -2 & -2 & -2 & -2 & -2 & -2 & -2 & -2 & 1 & 1 & 1 & 1 & 1 & 1 & 1 & 1 & -8 \\
-4 & 2 & -4 & 2 & 2 & 2 & 1 & 1 & 1 & 1 & 1 & -2 & 1 & -2 & 1 & -2 & 1 & -2 & 0 & 0 & 0 & 0 & 0 & 0 & 0 & 0 & 0 \\
0 & -2 & 0 & -2 & 2 & 2 & 1 & 1 & 1 & 1 & -1 & 0 & -1 & 0 & -1 & 0 & -1 & 0 & 0 & 0 & 0 & 0 & 0 & 0 & 0 & 0 & 0 \\
0 & 0 & 0 & 0 & 0 & 0 & -2 & 2 & -2 & 2 & 0 & 0 & 0 & 0 & 0 & 0 & 0 & 0 & 1 & -1 & 1 & -1 & 1 & -1 & 1 & -1 & 0 \\
0 & 0 & 0 & 0 & 0 & 0 & 0 & 0 & 0 & 0 & 0 & -2 & 0 & 2 & 0 & 2 & 0 & -2 & 1 & 1 & -1 & -1 & -1 & -1 & 1 & 1 & 0 \\
0 & 0 & 0 & 0 & 0 & 0 & 0 & 0 & 0 & 0 & -2 & 0 & 2 & 0 & 2 & 0 & -2 & 0 & 1 & -1 & -1 & 1 & -1 & 1 & 1 & -1 & 0 \\
0 & 0 & 0 & 0 & 0 & 0 & 1 & -1 & -1 & 1 & -1 & 0 & 1 & 0 & -1 & 0 & 1 & 0 & 0 & 0 & 0 & 0 & 0 & 0 & 0 & 0 & 0 \\
0 & 0 & 0 & 0 & 0 & 0 & -1 & -1 & 1 & 1 & 0 & 1 & 0 & -1 & 0 & 1 & 0 & -1 & 0 & 0 & 0 & 0 & 0 & 0 & 0 & 0 & 0 \\
0 & 0 & 0 & 0 & 0 & 0 & 0 & 0 & 0 & 0 & 1 & -1 & 1 & -1 & -1 & 1 & -1 & 1 & 0 & 0 & 0 & 0 & 0 & 0 & 0 & 0 & 0 \\
0 & 0 & 0 & 0 & 0 & 0 & 0 & 0 & 0 & 0 & 0 & 0 & 0 & 0 & 0 & 0 & 0 & 0 & 1 & -1 & 1 & -1 & -1 & 1 & -1 & 1 & 0
\end{pmatrix}. \tag{19}$$

The inverse matrix: $\boldsymbol{M}^{-1}$ is obtained by $\boldsymbol{M}^{-1} = \boldsymbol{M}^T \cdot \boldsymbol{l}_M^{-1}$ where $\boldsymbol{l}_M = \boldsymbol{M} \cdot \boldsymbol{M}^T$ and the equilibrium moment $\boldsymbol{m}^{(eq)}$ is obtained as $|\boldsymbol{m}^{(eq)}\rangle = \boldsymbol{M} \cdot |\boldsymbol{f}^{(eq)}\rangle$ with

$$f_\alpha^{(eq)} = w_\alpha \rho \left(1 + \frac{\boldsymbol{e}_\alpha \cdot \boldsymbol{u}}{{c_S}^2} + \frac{(\boldsymbol{e}_\alpha \cdot \boldsymbol{u})^2 - {c_S}^2 |\boldsymbol{u}|^2}{2c_S^4}\right), \tag{20}$$

where $\boldsymbol{u}$ is the fluid velocity.

Considering that the components of s_α corresponding to ρ and $\boldsymbol{j}$ need to be zero, the collision matrix $\widehat{\boldsymbol{S}}$ which is a diagonal 27×27 matrix may be written as

$$\widehat{\boldsymbol{S}} \equiv \mathrm{diag}(0, 0, 0, 0, s_4, s_5, s_5, s_7, s_7, s_7, s_{10}, s_{10}, s_{10}, s_{13}, s_{13}, s_{13}, s_{16}, s_{17}, s_{18}, s_{18}, s_{20}, s_{20}, s_{20}, s_{23}, s_{23}, s_{23}, s_{26}). \tag{21}$$

As in the D3Q15 and D3Q19 MRT-LBMs [12] the relation between the viscosities and the corresponding components of s_α are for the kinematic viscosity ν,

$$\nu = c_S^2 \left(\frac{1}{s_5} - \frac{1}{2}\right) \delta t = c_S^2 \left(\frac{1}{s_7} - \frac{1}{2}\right) \delta t, \tag{22}$$

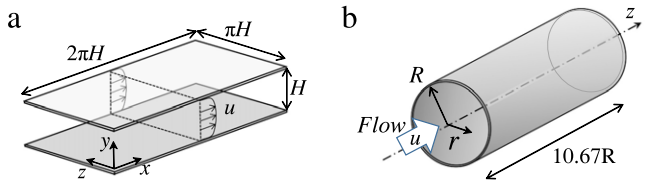

Fig. 2. Test flow geometries and computational domains: (a) channel flow, (b) pipe flow.

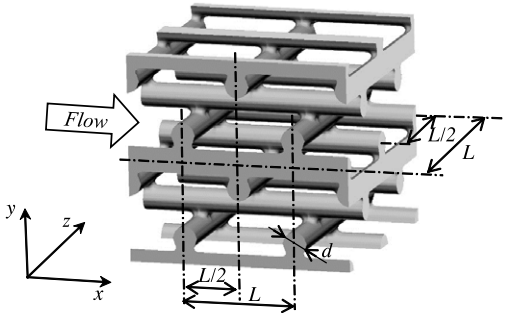

Fig. 3. Structure of the model porous medium; $L = 4.33d$, $d = 3$ mm, the porosity is 0.8.

for the bulk viscosity ζ,

$$\zeta = \frac{5 - 9c_S^2}{9}\left(\frac{1}{s_4} - \frac{1}{2}\right)\delta t, \tag{23}$$

where s_4, s_5 and s_7 are the relaxation factors for the kinetic energy and the second order tensors. The relaxation factors need to satisfy $0 < s_\alpha < 2$ for stability. As discussed by Lallemand and Luo [15], although the remaining relaxation factors have effects on higher order terms, they can be adjusted without having any effect on the transport coefficients. Hence, to attain numerical stability, d'Humiéres et al. [12] obtained their sub-optimal relaxation factors as the result of a compromise through linear analyses. Although recent studies [16–18] discussed on the relaxation factors through further consideration, to obtain the stable solutions for the presently focused flows, a large number of searches in a parameter space in this study have given a set of relaxation factors as

$$\begin{aligned} &s_4 = 1.54, \quad s_{10} = 1.5, \quad s_{13} = 1.83, \quad s_{16} = 1.4, \quad s_{17} = 1.61, \\ &s_{18} = s_{20} = 1.98, \quad s_{23} = s_{26} = 1.74. \end{aligned} \tag{24}$$

Note that those values are sub-optimal ones and the other sets of values are also possible. For incompressible fluids, the bulk viscosity may not be important and thus the factor related to it is set to be constant. (d'Humiéres et al. [12] also proposed constant values: 1.6 and 1.19 for the D3Q15 and D3Q19 models, respectively.) When the bounce back boundary condition is applied as the non-slip wall boundary, Ginzburg et al. [31] led the relation between the relaxation factors related to energy fluxes and the kinematic viscosity. It can be written in the present system as

$$s_{10} = \frac{8\,(2 - s_5)}{8 - s_5}. \tag{25}$$

Hence, if the kinematic viscosity is given, by Eqs. (22) and (25), s_{10} is obtained. However, it has been experienced that solutions are not always stable with such values for s_{10}. Thus, in the present study, the constant value is applied to s_{10} as in Eq. (24). (d'Humiéres et al. [12] also applied the constant value to the relaxation factor for energy fluxes.)

3. Numerical simulations for turbulent flows

For evaluation of the present D3Q27 MRT LBM, three test cases are considered. They are fully developed channel, pipe and porous medium flows whose geometries are illustrated in Fig. 2(a), (b) and Fig. 3, respectively. The porous medium consists of frameworks of circular rods. Both geometries of the pipe and the porous medium include round wall boundaries which induce anomaly in the solution by the D3Q15 and D3Q19 models [23–25,27]. Although direct numerical simulation (DNS) is applied to the channel flow, to simulate pipe and porous medium flows, large eddy simulation (LES) using the sub-grid-scale (SGS) eddy viscosity model is applied. The numerical description of the SGS model is as follows.

3.1. SGS model

The SGS stress R_{ij} appearing in the filtered momentum equation is modelled by the eddy viscosity model as

$$R_{ij} = -\nu_{sgs}\left(\frac{\partial\langle u_i\rangle}{\partial x_j} + \frac{\partial\langle u_j\rangle}{\partial x_i}\right) + \frac{2}{3}k_{sgs}\delta_{ij}, \tag{26}$$

where $\langle u_i\rangle$ denotes the filtered velocity component, k_{sgs} is the SGS turbulent energy and ν_{sgs} is the SGS eddy viscosity.

For ν_{sgs}, the so called wall-adapting local eddy-viscosity (WALE) model [32] is applied in the present study. It employs the strain tensors:

$$\langle S_{ij}\rangle = \frac{1}{2}\left(\frac{\partial\langle u_i\rangle}{\partial x_j} + \frac{\partial\langle u_j\rangle}{\partial x_i}\right), \qquad \langle g_{ij}\rangle = \frac{\partial\langle u_i\rangle}{\partial x_j}, \tag{27}$$

and

$$\mathcal{S}_{ij}^d = \frac{1}{2}\left(\langle g_{ij}\rangle^2 + \langle g_{ji}\rangle^2\right) - \frac{1}{3}\delta_{ij}\langle g_{kk}\rangle^2, \tag{28}$$

with $\langle g_{ij}\rangle^2 = \langle g_{ik}\rangle\langle g_{kj}\rangle$, to consider wall effects. Then, the SGS eddy viscosity is expressed as

$$\nu_{sgs} = C_w\Delta^2\frac{\left(\mathcal{S}_{ij}^d\mathcal{S}_{ij}^d\right)^{3/2}}{\left(\langle S_{ij}\rangle\langle S_{ij}\rangle\right)^{5/2} + \left(\mathcal{S}_{ij}^d\mathcal{S}_{ij}^d\right)^{5/4}}, \tag{29}$$

where Δ is the grid spacing (δx in the LBM) and the SGS eddy viscosity coefficient $C_w = 0.1$ [33]. To keep consistency, all the tensors consisting of velocity gradients are obtained by the central difference in the velocity field.

Coupled with the kinematic viscosity, this SGS eddy viscosity is related to s_5 and s_7 as

$$(\nu + \nu_{sgs}) = c_S^2\left(\frac{1}{s_5} - \frac{1}{2}\right)\delta t = c_S^2\left(\frac{1}{s_7} - \frac{1}{2}\right)\delta t. \tag{30}$$

It is well known that the LBE converges to the Navier–Stokes equation by the Chapman–Enskog expansion with the second order accuracy. However, the pressure term there is strictly for the static pressure not for the turbulent pressure (: the static pressure plus turbulent energy). Thus, when the LES is considered in the framework of the LBM, it is necessary to consider separately the SGS turbulent energy k_{sgs} appearing in Eq. (26). In the present study, following Inagaki et al. [34], k_{sgs} is estimated as

$$k_{sgs} = C_{kes}\sum_{i=1}^{3}\left(\langle\hat{u}_i\rangle - \langle u_i\rangle\right)^2, \tag{31}$$

where the model coefficient is set to $C_{kes} = 1.0$ and the notation $\hat{()}$ denotes the filtering operator for which the Simpson rule is adopted. It corresponds to space filtering with a filter width of 2Δ. This estimation procedure is based on an idea similar to the scale similarity proposed by Bardina et al. [35]. Thus, $\langle\hat{u}_i\rangle$ is expressed as

$$\langle\hat{u}_i\rangle = \frac{1}{2}\langle u_i\rangle + \frac{\langle u_i^E\rangle + \langle u_i^W\rangle + \langle u_i^N\rangle + \langle u_i^S\rangle + \langle u_i^T\rangle + \langle u_i^B\rangle}{12}, \tag{32}$$

where u_i^E, u_i^W, $u_i^N\cdots$ are the velocity components of the neighbouring nodes of node i. Applying the above form to Eq. (31), k_{sgs} can be calculated and included in the body force term as

$$F_\alpha = \frac{\rho w_\alpha\delta t}{c_S^2}\boldsymbol{e}_\alpha\cdot\left(-\frac{2}{3}\nabla k_{sgs}\right). \tag{33}$$

3.2. Validation

For the DNS of the fully developed channel flow, the case at the friction Reynolds number (based on the friction velocity u_τ and a half of the channel height $(H/2)$) $\mathrm{Re}_\tau = 180$ is considered. The lattice nodes of $1539\times240\times750$ are applied to the computational domain of $2\pi H(x)\times H(y)\times\pi H(z)$. For the wall boundary condition, the half-way bounce back scheme is used whereas the periodic conditions are applied to the inlet and outlet boundaries and to the spanwise boundaries.

Fig. 4 compares turbulence statistical quantities with the DNS database by the spectral method of Kim et al. [36]. The streamwise mean velocity U^+, Reynolds shear $-\overline{uv}^+$ and normal stresses $\overline{u_i^2}$ profiles are compared in Fig. 4(a)–(c). The budget terms of the turbulent kinetic energy k are compared in Fig. 4(d). Here, $(\cdot)^+$ means a normalized value by the friction velocity. It is seen that each agreement between the present D3Q27 MRT model and the spectral method is almost

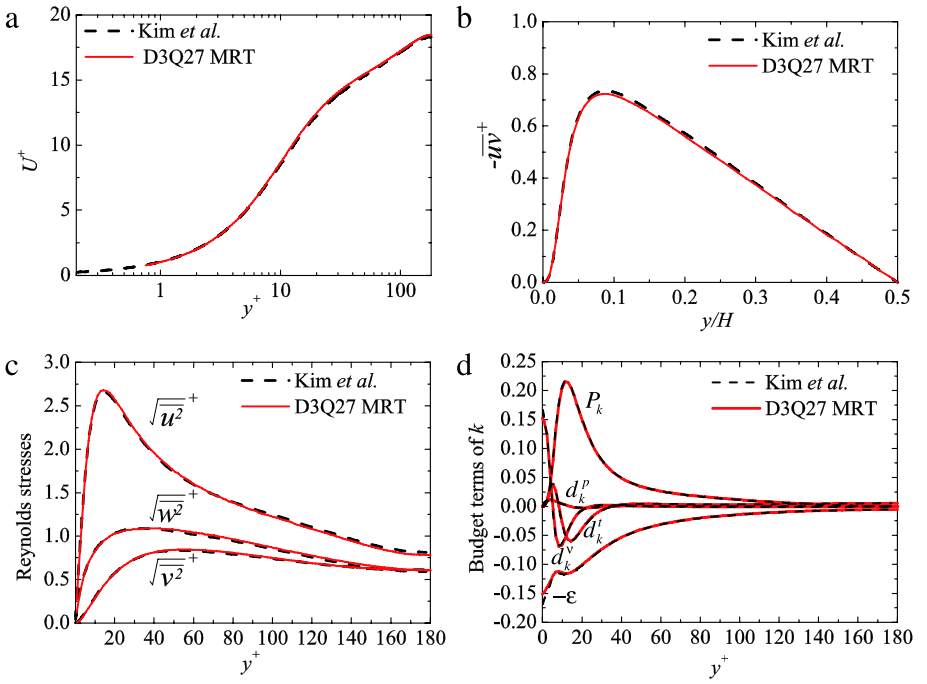

Fig. 4. Comparison of the statistical turbulent quantities of the channel flow at $\mathrm{Re}_\tau = 180$ between different DNS results: (a) streamwise mean velocity, (b) Reynolds shear stress, (c) Reynolds normal stresses, (d) budget terms of the turbulent kinetic energy k. The production, dissipation, viscous diffusion, turbulent diffusion and pressure diffusion terms of k correspond to P_k, ε, d_k^v, d_k^t and d_k^p, respectively.

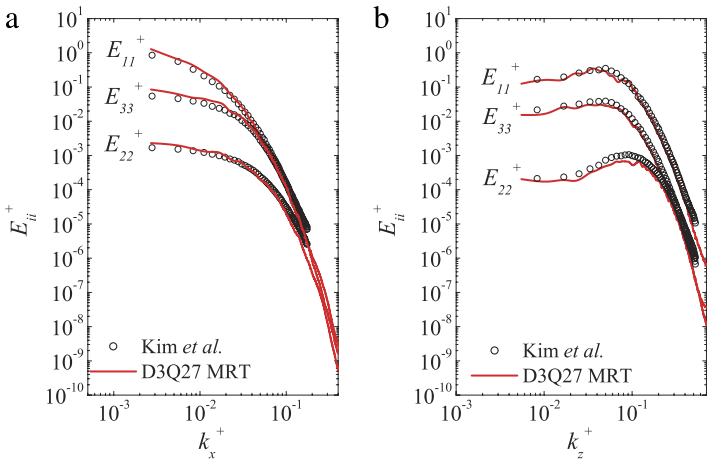

Fig. 5. One-dimensional energy spectra at $y^+ \simeq 5$: (a) streamwise direction, (b) spanwise direction. Wave numbers k_x and k_z are in the streamwise and spanwise directions. E_{11}, E_{22} and E_{33} correspond to the streamwise, wall normal and spanwise components, respectively. The profiles of the present study are at $y^+ = 5.32$ while those by Kim et al. [36] are at $y^+ = 5.39$.

perfect. Moreover, as shown in Fig. 5, one-dimensional energy spectrum distributions are also in good agreement for both the streamwise and spanwise directions. Thus, it is confirmed that the present scheme is as reliable as the spectral method for DNSs of turbulent flows.

For the LES of the fully developed pipe flow at $\mathrm{Re} = 5400$, lattice nodes of 400 (streamwise) $\times$ 75 $\times$ 75, whose 75% are occupied by the fluid, are used. This lattice is finer than that confirmed to be fine enough in the pipe flow LES study by Kang and Hassan [24]. The Reynolds number Re is based on the bulk velocity U_b and the pipe diameter $D = 2R$ as $\mathrm{Re} = U_b D/\nu$ while the friction Reynolds number based on the friction velocity u_τ and the pipe diameter is $\mathrm{Re}_\tau = 360$. For the wall boundary condition, the linearly interpolated bounce back scheme of Pan et al. [13] is used whereas the periodic conditions are applied to the inlet and outlet boundaries.

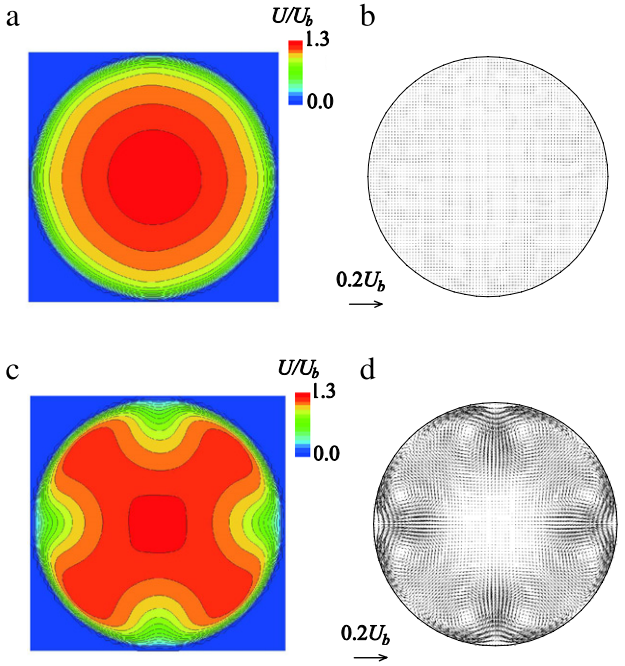

Fig. 6. Mean velocity profiles of the pipe flow at Re = 5400 by LES: (a) contours of streamwise mean velocity by the D3Q27 MRT LBM, (b) sectional secondary flow vectors by the D3Q27 MRT LBM, (c) contours of streamwise mean velocity by the D3Q19 MRT LBM, (b) sectional secondary flow vectors by the D3Q19 MRT LBM.

Fig. 6 shows the mean velocity profiles by the present D3Q27 MRT model comparing them to those by the D3Q19 MRT model. Although this comparison looks somewhat reproduction of the well discussed feature of the LBM, such a test case is still worth discussing for the newly developed scheme. Obviously, the D3Q27 MRT model reproduces an axisymmetric flow profile fairly satisfactorily without visible secondary flows. However, when the D3Q19 MRT model is applied, as reported by Kang and Hassan [24], unphysically skewed flow profiles are produced as shown in Fig. 6(c) and (d). Since such skewness comes from the non-axisymmetric error terms including the Reynolds stress in the LBE as discussed in [27], it tends to be amplified as the Reynolds number increases. Fig. 7 compares turbulence statistical quantities such as the streamwise mean velocity U^+, Reynolds shear $-\overline{uv}^+$ and normal stresses $\overline{u_i^2}$ ($:\overline{u^2}$, $\overline{v^2}$ and $\overline{w^2}$ correspond to the streamwise, radial and circumferential components, respectively) with the classical DNS data by Unger and Friedrich [37]. Although the agreement is not perfect, the present LES results by the D3Q27 MRT model well accord with the DNS data.

For the LES of the model porous medium flows, lattice nodes of $53(x) \times 49(y) \times 53(z)$, whose 80% are for the fluid phase, are used for the unit cell of the structure. Note that the unit cell is the minimum structure that forms the whole structure by recursively appearing in each direction. (The volume shown in Fig. 3 consists of eight unit cells.) The lattice nodes are confirmed to be enough by comparing the results by $78(x) \times 72(y) \times 78(z)$ at the highest Reynolds number case. Indeed, the volume-averaged grid-scale turbulent energy differs less than 5% from that by the finer lattice arrangement. As in the pipe flow, the linearly interpolated bounce back scheme is applied to the solid wall boundaries. A pressure difference between the inlet and outlet boundaries is imposed whereas the periodic conditions are applied to the domain boundaries in the other directions.

This flow case may be a severer flow case since the flow domain includes many round shaped obstacles and flow becomes unstable at substantially low Reynolds number. (Our experience hence suggested that stable solutions were not obtained by the lattice BGK model for this case.) Indeed, Dybbs and Edwards [38] reported experimental results of flows in complex rod bundles which were similar to the present case concluding that the flow started to be unstable at the Reynolds number of 150–300 and eventually became turbulent from Re = 350.

Fig. 8 shows iso-surfaces of the second invariant of the grid-scale velocity gradient tensor II $\left(= -\frac{1}{2}\frac{\partial\langle u_i\rangle}{\partial x_j}\frac{\partial\langle u_j\rangle}{\partial x_i}\right)$ for $II = 1.7 \times 10^4$ coloured by the values of vorticity ω_z. The Reynolds number is Re = 1300 that is based on the Darcy velocity U_d and the effective mean pore diameter $D_p = 2.7d$ which is calculated from the spheroid volume circumscribed by the rods composing the porous medium by using the Sauter mean diameter method. The values of II and ω_z are also normalized by U_d and D_p. The figure clearly indicates that the flow field is substantially turbulent consisting of vortices which are shed from the cylinders and impinging onto the next cylinders. Such turbulent mixing causes high pressure drops as the Reynolds number increases as shown in Fig. 9. Fig. 9 validates the present results comparing with the experimental data by Iida et al. [39]. It is clear that the present simulation by the D3Q27 MRT model well reproduces the experimental data though available experimental data for the fully developed turbulence regime are the pressure drops only.

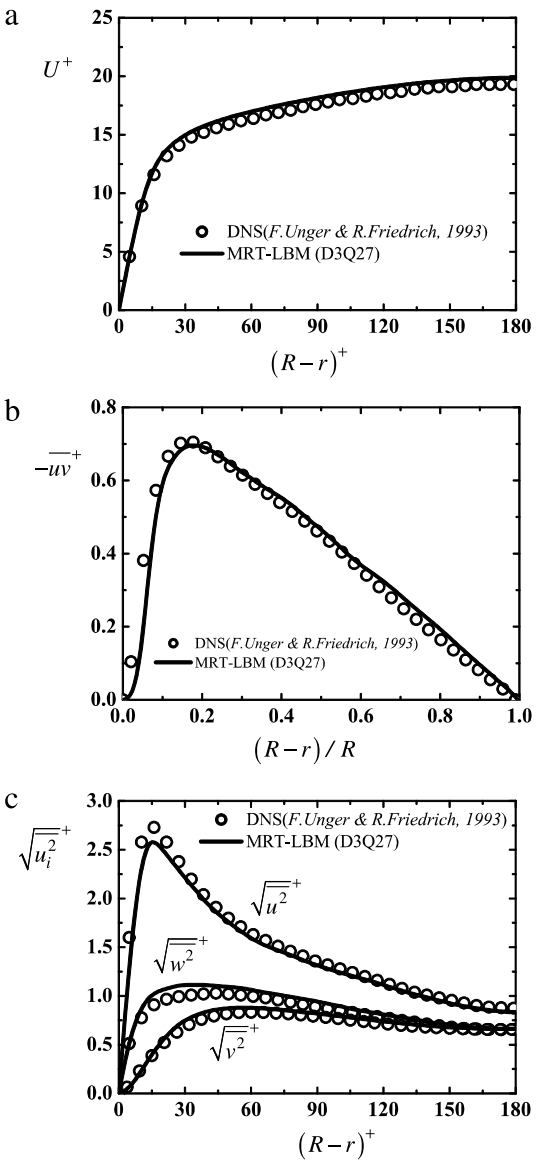

Fig. 7. Comparison of the statistical turbulent quantities of the pipe flow at Re = 5400 between the present LES and the DNS data: (a) streamwise mean velocity, (b) Reynolds shear stress, (c) Reynolds normal stresses; u, v and w are the streamwise, radial and circumferential components, respectively.

4. Conclusions

In the present study, a multiple-relaxation-time lattice Boltzmann equation for the D3Q27 discrete velocity model is developed. The proposed scheme is successfully validated in the application to the DNS of a fully developed turbulent channel flow that is the standard benchmark case of wall turbulence. It is confirmed that the proposed scheme performs as reliable as the spectral method for turbulence simulations. For pipe flows, the present scheme combined with the SGS model produces satisfactorily axisymmetric turbulent flow profiles. The highly complex turbulent flows inside the model porous medium whose structure consists of frameworks of circular rods are stably simulated by the present scheme. The overall pressure drops of the model porous medium are well predicted by the present model. Therefore, the present D3Q27 MRT LBM is successfully applicable to simulations for complex turbulent flows.

Acknowledgements

The technical support by Dr. M. Kaneda is appreciated. A part of this study was financially supported by the research grant (No. 24360073) of the JSPS Japan.

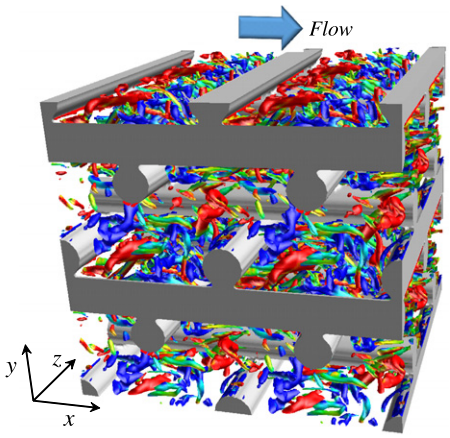

Fig. 8. Iso-surfaces of the second invariant of the grid-scale velocity gradient tensor at $II = 1.7 \times 10^4$ which are coloured based on the local values of vorticity ω_z at Re = 1300; blue–red colours correspond to $-5 \leq \omega_z \leq 5$. (For interpretation of the references to colour in this figure legend, the reader is referred to the web version of this article.)

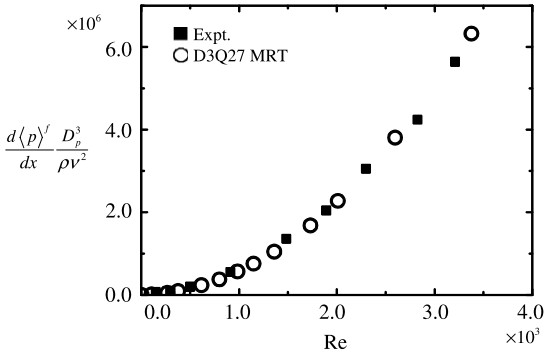

Fig. 9. Pressure drops in the model porous medium; $\langle p \rangle^f$ denotes the fluid-phase volume-averaged pressure.

References

[1] P.L. Bhatnagar, E.P. Gross, M. Krook, A model for collision processes in gases. I. Small amplitude processes in charged and neutral one-component systems, Phys. Rev. 94 (1954) 511–525.
[2] C.K. Aidun, J.R. Clausen, Lattice Boltzmann method for complex flows, Annu. Rev. Fluid Mech. 42 (2010) 439–472.
[3] K. Suga, Lattice Boltzmann methods for complex micro-flows: applicability and limitations for practical applications, Fluid Dynam. Res. 45 (2013) 034501.
[4] J.G.M. Eggels, Direct and large-eddy simulation of turbulent fluid flow using the lattice Boltzmann scheme, Int. J. Heat Fluid Flow 17 (1996) 307–323.
[5] D. Yu, S.S. Girimaji, L.-S. Luo, DNS and LES of decaying isotropic turbulence with and without frame rotation using lattice Boltzmann method, J. Comput. Phys. 209 (2005) 599–616.
[6] D.Z. Yu, S.S. Girimaji, Direct numerical simulations of homogeneous turbulence subject to periodic shear, J. Fluid Mech. 566 (2006) 117–151.
[7] L. Djenidi, Lattice-Boltzmann simulation of grid-generated turbulence, J. Fluid Mech. 552 (2006) 13–35.
[8] Y.-H. Dong, P. Sagaut, A study of time correlations in lattice Boltzmann-based large-eddy simulation of isotropic turbulence, Phys. Fluids 20 (2008) 035105.
[9] H. Yu, L.-S. Luo, S.S. Girimaji, LES of turbulent square jet flow using an MRT lattice Boltzmann model, Comput. Fluids 35 (2006) 957–965.
[10] P. Sagaut, Toward advanced subgrid models for lattice-Boltzmann-based large-eddy simulation: theoretical formulations, Comput. Math. Appl. 59 (2010) 2194–2199.
[11] D. d'Humiéres, Generalized lattice Boltzmann equations, in: D.D. Shizgal, D.P. Weaver (Eds.), Rarefied Gas Dynamics: Theory and Simulations, in: Prog. Aeronaut. Astronaut., vol. 159, 1992, pp. 450–458.
[12] D. d'Humiéres, I. Ginzburg, M. Krafczyk, P. Lallemand, L.-S. Luo, Multiple-relaxation-time lattice Boltzmann models in three dimensions, Phil. Trans. R. Soc. A 360 (2002) 437–451.
[13] C. Pan, L.-S. Luo, C.T. Miller, An evaluation of lattice Boltzmann schemes for porous medium flow simulation, Comput. Fluids 35 (2006) 957–965.
[14] K.N. Premnath, M.J. Pattison, S. Banerjee, Dynamic subgrid scale modeling of turbulent flows using lattice Boltzmann method, Physica A 388 (2009) 2640–2658.
[15] P. Lallemand, L.-S. Luo, Theory of the lattice Boltzmann method: dispersion, isotropy, Galilean invariance, and stability, Phys. Rev. E 61 (2000) 6546–6562.
[16] F. Dubois, P. Lallemand, Quartic parameters for acoustic applications of lattice Boltzmann scheme, Comput. Math. Appl. 61 (12) (2011) 3404–3416.
[17] A. Augier, F. Dubois, B. Graille, P. Lallemand, On rotational invariance of lattice Boltzmann schemes, Comput. Math. Appl. 67 (2) (2014) 239–255.
[18] P.J. Dellar, Lattice Boltzmann algorithms without cubic defects in Galilean invariance on standard lattices, J. Comput. Phys. 259 (2014) 270–283.
[19] Y.H. Qian, Y. Zhou, Complete Galilean-invariant lattice BGK models for the Navier–Stokes equation, Europhys. Lett. 42 (1988) 359–364.
[20] X.B. Nie, X. Shan, H. Chen, Galilean invariance of lattice Boltzmann methods, Europhys. Lett. 81 (2008) 34005.
[21] H. Chen, S. Orszag, Moment isotropy and discrete rotational symmetry of two-dimensional lattice vectors, Phil. Trans. R. Soc. A 369 (2011) 2176–2183.
[22] G. Silva, V. Semiao, Truncation errors and the rotational invariance of three-dimensional lattice models in the lattice Boltzmann method, J. Comput. Phys. 269 (2014) 259–279.

[23] G. Mayer, G. Házi, Direct numerical and large eddy simulation of longitudinal flow along triangular array of rods using the lattice Boltzmann method, Math. Comput. Simul. 72 (26) (2006) 173–178.
[24] S.K. Kang, Y.A. Hassan, The effect of lattice models within the lattice Boltzmann method in the simulation of wall-bounded turbulent flows, J. Comput. Phys. 232 (1) (2013) 100–117.
[25] S. Geller, S. Uphoff, M. Krafczyk, Turbulent jet computations based on MRT and cascaded lattice Boltzmann models, Comput. Math. Appl. 65 (12) (2013) 1956–1966.
[26] D.J. Holdych, D.R. Noble, J.G. Georgiadis, R.O. Buckius, Truncation error analysis of lattice Boltzmann methods, J. Comput. Phys. 193 (2) (2004) 595–619.
[27] Y. Kuwata, K. Suga, Anomaly of the lattice Boltzmann methods in three-dimensional cylindrical flows, J. Comput. Phys. 280 (2015) 563–569.
[28] K.N. Premnath, S. Banerjee, On the three-dimensional central moment lattice Boltzmann method, J. Stat. Phys. 143 (2011) 747–794.
[29] S. Chen, G.D. Doolen, Lattice Boltzmann method for fluid flows, Annu. Rev. Fluid Mech. 30 (1998) 329–364.
[30] Z. Guo, C. Zheng, B. Shi, Discrete lattice effects on forcing term in the lattice Boltzmann method, Phys. Rev. E 65 (2002) 04638.
[31] I. Ginzburg, D. d'Humiéres, Multireflection boundary conditions for lattice Boltzmann models, Phys. Rev. E 68 (2003) 066614.
[32] F. Nicoud, F. Ducros, Subgrid-scale stress modelling based on the square of the velocity gradient tensor, Flow Turbul. Combust. 62 (1999) 183–200.
[33] J. Fröhlich, C.P. Mellen, W. Rodi, L. Temmerman, M.A. Leschziner, Highly resolved large-eddy-simulation of separated flow in a channel with streamwise periodic constrictions, J. Fluid Mech. 526 (2005) 19–66.
[34] M. Inagaki, M. Nagaoka, N. Horinouchi, K. Suga, Large eddy simulation analysis of engine steady intake flows using a mixed-time-scale subgrid-scale model, Int. J. Engine Res. 11 (2010) 229–241.
[35] J. Bardina, J.H. Ferziger, W.C. Reynolds, Improved turbulence models based on large eddy simulation of homogenous, incompressible, turbulent flows, Tech. Rep. TF-10, Thermosciences Division, Department of Mechanical Engineeering, Stanford University, Stanford, California, 1983.
[36] J. Kim, P. Moin, R. Moser, Turbulence statistics in fully developed channel flow at low Reynolds number, J. Fluid Mech. 177 (1987) 133–166.
[37] F. Unger, R. Friedrich, Fully developed turbulent pipe flow, Tech. Rep. DNS Database of Turbulence and Heat Transfer, Code number: PI12 PG.WL1, Department of Mechanical Engineering, The University of Tokyo, Tokyo, Japan, 1993.
[38] A. Dybbs, R.V. Edwards, A new look at porous media fluid mechanics-Darcy to turbulent, in: J. Bear, M.Y. Corapcioglu (Eds.), Fundamentals of Transport Phenomena in Porous Media, in: NATO ASI Series, vol. 82, Springer, Netherlands, 1984, pp. 199–256.
[39] T. Iida, A. Taneo, M. Kaneda, K. Suga, PIV measurements of interface turbulence over hetero-porous media, J. Phys. Conf. Ser. 530 (2014) 012058.